Journal of Materials Chemistry C

ROYAL SOCIETY OF CHEMISTRY

PAPER

Published on 10 August 2026
Licensed under CC-BY 4.0

Check for updates

Cite this: DOI: 10.1039/d6tc01758d

Site-selective cation distribution and structural distortion in $Y_3Al_{5-x}Ga_xO_{12}$:Pr garnet phosphors: a multi-analytical investigation

Maria Luisa Saladino, [ab] Alberto Spinella, [c] Paulina Bukowska, *[d] Rico Friedrich, [ef] Małgorzata Sójka [g] and Eugeniusz Zych [de]

Received 29th May 2026,
Accepted 6th August 2026

DOI: 10.1039/d6tc01758d

rsc.li/materials-c

This study presents a comprehensive investigation into the site-selective distribution of Ga^{3+} and Al^{3+} cations within the tetrahedral (16d) and octahedral (24f) sites of the $Y_3Al_{5-x}Ga_xO_{12}$:Pr garnet series. By integrating X-ray powder diffraction (XRD), solid-state NMR (nuclear magnetic resonance) spectroscopy, and density functional theory (DFT) calculations, we elucidated the site occupancy preferences across the compositional range. Our results provide a consistent structural model, demonstrating that Ga^{3+} ions exhibit a clear preference for tetrahedral sites over octahedral ones. Furthermore, we reveal that while XO_6 octahedra undergo pronounced structural distortion in mixed Al–Ga compositions, the XO_4 tetrahedra remain remarkably resistant to deformation. These findings establish a fundamental framework for structural modeling and provide critical insights for tailoring the luminescence performance of garnet-based phosphors through strategic site engineering. The methodologies and structural principles derived here are readily applicable to the design of other complex mixed-cation host lattices.

1. Introduction

Yttrium aluminum garnet ($Y_3Al_5O_{12}$, YAG) and yttrium gallium garnet ($Y_3Ga_5O_{12}$, YGG), as well as their mixed forms ($Y_3Al_{5-x}Ga_xO_{12}$, YAGG) with different Al:Ga ratios, are thoroughly investigated because of their attractive, technologically useful optical properties if doped with rare earths or transition metal ions. Varying the Al:Ga ratio allows fine-tuning of their spectroscopic properties while maintaining the garnet crystal structure. Such phosphors are of great interest for lasers, white or infrared LEDs, scintillators, sensors, (nano)thermometers, and persistent luminescence materials.[1–4]

Polycrystalline YAGG co-doped with various lanthanide ions has been the focus of extensive research by Tanabe *et al.*[5–7] Although such garnets are known for their high thermodynamic stability, their optical properties and potential applications remain highly dependent not only on the choice of doping elements but also on the synthesis methods.[8,9] These factors can significantly affect particle size, morphology, and defect types, as well as their populations and distributions at the microscopic scale.[10] Yet another way to shape the luminescence of such garnets is to make single-crystalline films whose properties differ significantly from those of classic single crystals due to a relatively low formation temperature, around 1000 °C.[8,11,12] In recent years, particular emphasis has been placed on exploring the mechanisms underlying persistent luminescence (PersL) phenomena and thermometry, both of which are closely related to specific particle size, aggregation, and especially lattice defects – whether extrinsic or intrinsic.[13–15]

Garnets crystallize in the cubic crystal system with the $Ia\bar{3}d$ space group, and their general formula is $A_3B_2C_3O_{12}$, where A corresponds to a dodecahedral (D_2) site with 8-fold coordination, B is an octahedral (O_h) site with 6-fold coordination, and C is a tetrahedral (T_d) site showing 4-fold coordination, see Fig. 1. In the YAGG structure, Y^{3+} ions occupy the D_2 site, while the smaller Al^{3+} and Ga^{3+} ions fit into the O_h (Al^{3+}: 0.535 and Ga^{3+}: 0.62 Å) and T_d (Al^{3+}: 0.39 and Ga^{3+}: 0.47 Å)[16] sites. As a result, the dopant Rare Earth ion typically replaces the Y^{3+} ion in the dodecahedral position due to the similarity in ionic radii. However, small transition-metal ions, for example, Cr^{3+}, prefer the T_d position.[17–19] Notably, YAG, LuAG, and similar garnets

[a] Department of Biological, Chemical and Pharmaceutical Science and Technology, University of Palermo, Viale delle Scienze Bld. 17, Palermo I-90128, Italy
[b] National Research Council of Italy, Institute for Chemical and Physical Processes, IPCF-Messina, Viale Ferdinando Stagno d'Alcontres 37, Messina I-98158, Italy
[c] ATeN Center, University of Palermo, Viale delle Scienze Bld. 18, Palermo I-90128, Italy
[d] Faculty of Chemistry, University of Wrocław, F. Joliot-Curie Street, 50-383 Wrocław, Poland. E-mail: paulina.bukowska@uwr.edu.pl
[e] Helmholtz-Zentrum Dresden-Rossendorf, Dresden 01328, Germany
[f] Theoretical Chemistry, Technische Universität Dresden, Dresden 01069, Germany
[g] Department of Chemistry, University of Houston, Houston, Texas 77204, USA

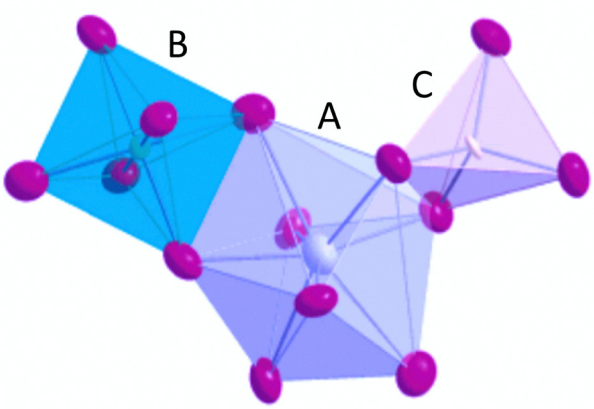

Fig. 1 Simple visualization of the three metal sites in $Y_3Al_5O_{12}$ garnet. A is a dodecahedral site with coordination number CN = 8 occupied by Y^{3+}, B is an octahedral site with CN = 6 occupied by Al^{3+}, and C is a tetrahedral site, CN = 4, also occupied by Al^{3+}.

are known to generate antisite defects when Y^{3+} and Al^{3+} mutually replace their positions in crystals.[20–22] They are formed, however, when the fabrication temperature is high, above about 1300 °C. Therefore, antisites are especially abundant in single crystals grown by the Czochralski method close to 2000 °C and are practically absent in single-crystalline films produced by liquid-phase epitaxy, which requires temperatures around 1000 °C only, as mentioned above.

Compared to YAG, the presence of gallium in a mixed YAGG host can affect the optical properties. This happens because it necessarily creates a distortion in the lattice and reduces the forbidden bandgap energy, mainly by lowering the bottom of the conduction band.[23–27] Replacing Al with Ga also diminishes the host phonon energies.[15] All these effects are known to influence – sometimes profoundly – luminescent processes and mechanisms of energy dissipation in and by the specific compositions.[15,28,29] Similar observations were proved in $Lu_3Al_{5-x}Ga_xO_{12}:Ce^{3+}$ phosphors.[30,31]

Consequently, the distribution of Ga^{3+} ions between T_d (AlO_4) and O_h (AlO_6) sublattices – whether random or preferential – is a critical factor in the design of phosphors based on $Y_3Al_{5-x}Ga_xO_{12}$ and related garnet hosts. Luminescence, as a radiative de-excitation process, is intrinsically linked to non-radiative relaxation pathways of excited charge carriers. The balance between these competing (radiative and nonradiative) processes governs key phosphor characteristics, including emission efficiency and emission wavelength (energy).

One of the dominant nonradiative relaxation mechanisms is multiphonon relaxation between neighboring electronic levels. It depends primarily on the phonon energy available in the system. At a specified temperature, the nonradiative relaxation rate, $W(T)$, is quantified by eqn (1):[32,33]

$$W(T) = W(0)(n+1)^p, \quad (1)$$

where $W(0)$ is nonradiative rate at the $T \rightarrow 0$ K limit, $n = \left[\exp\left(\frac{h\nu}{kT}\right) - 1\right]^{-1}$, and $p = \frac{\Delta E}{h\nu}$. Here, ΔE denotes the energy gap between the involved electronic levels, while $h\nu$ represents the energy of the highest-energy phonons available in the host lattice. Note that n is the Bose–Einstein phonon occupation number, representing the (average) population of lattice vibrational modes with energy $h\nu$ at temperature T. It reflects the thermal availability of phonons that mediate multiphonon non-radiative relaxation. With increasing temperature or decreasing phonon energy, n increases, thereby enhancing the probability of nonradiative decay.

From the above, it follows that when the electronic levels under consideration are bridged by approximately five phonons ($\Delta E \approx 5h\nu$), radiative and nonradiative relaxation of the upper level occurs with comparable probabilities. Consequently, a smaller energy separation of electronic levels favors non-radiative multiphonon relaxation, whereas a larger separation enhances radiative decay.

In the $Y_3Al_{5-x}Ga_xO_{12}$ series, the relevant vibrational modes originate from different coordination polyhedra and can be ordered by decreasing phonon energy as follows: AlO_4 (~770–900 cm^{-1}) > AlO_6 (~670–750 cm^{-1}) ≈ GaO_4 (~650–750 cm^{-1}) > GaO_6 (~550–650 cm^{-1}).[15] Therefore, it is of particular importance whether Ga incorporation into the lattice preferentially reduces the population of AlO_4 or AlO_6 vibrational units.

Thus, the smaller and more rigid AlO_4 tetrahedra, characterized by shorter Al–O bonds, generate higher-energy phonons than the AlO_6 octahedra and therefore define the upper phonon energy limit of the $Y_3Al_{5-x}Ga_xO_{12}$ host lattice. Substitution of Al^{3+} by the heavier Ga^{3+} at tetrahedral sites leads to a pronounced reduction in phonon energies relative to those associated with AlO_4 units. Consequently, preferential occupation of tetrahedral sites by Ga^{3+} ions suppresses the highest-energy phonon modes of the host lattice more effectively than a random distribution over both coordination environments. Since these high-energy phonons predominantly govern non-radiative energy dissipation *via* multiphonon relaxation, T_d-site-selective/preferential Ga^{3+} incorporation results in a more efficient reduction of nonradiative losses than random substitution.

Previous studies have addressed this issue. However, a consistent picture of the preferential occupancy of octahedral (O_h, 16a) and tetrahedral (T_d, 24d) sites by Al^{3+} and Ga^{3+} ions remains elusive in both $Y_3Al_{5-x}Ga_xO_{12}$ and $Lu_3Al_{5-x}Ga_xO_{12}$ series Fu *et al.* investigated powders prepared by solid-state reaction and reported that Ga^{3+} preferentially occupies the larger O_h sites, entering the T_d sites only after saturation of the octahedral positions.[34] Similarly, Jiang *et al.* argued that Ga^{3+} incorporation into T_d sites becomes increasingly unfavorable once three or more Al^{3+} ions are substituted, potentially promoting the formation of secondary phases.[35] In contrast, our previous work examined the influence of annealing at temperatures up to 1000 °C on Ga^{3+} site occupancy in $Y_3Al_{5-x}Ga_xO_{12}$ and showed that, within this temperature range, Al/Ga redistribution between O_h and T_d sites remains largely random after annealing at 890 °C, with only a minor increase in Ga^{3+} occupancy of T_d sites observed at 1000 °C.[36] Furthermore, Gautier *et al.* employed NMR and X-ray absorption spectroscopy

 This journal is © The Royal Society of Chemistry 2026

to demonstrate a preference of Ga^{3+} for T_d sites over O_h sites in sol–gel-derived $Y_3Al_{5-x}Ga_xO_{12}$ powders.[37]

On the other hand, Laguta *et al.* demonstrated by solid-state NMR that in $Y_3Al_{5-x}Ga_xO_{12}$:Ce, Ga^{3+} ions preferentially occupy the tetrahedral sites of the garnet lattice, whereas Al^{3+} ions preferentially reside in octahedral sites, despite the smaller ionic radius of Al^{3+} compared to Ga^{3+}.[29] It should be noted that these results were obtained for single crystals grown at temperatures close to the YAG melting point ($\sim$1970 °C). The authors attributed this behavior to the stronger covalent character of the Ga–O bond relative to the Al–O bond, as well as to reduced cation–cation repulsive interactions.

Consistent conclusions were reported for $Lu_3Al_{5-x}Ga_xO_{12}$ garnets. Yu *et al.* combined NMR spectroscopy with density functional theory calculations and found that Ga^{3+} preferentially occupies T_d sites.[38] Similarly, Babin *et al.* used solid-state NMR to quantify the fractional occupancies of Ga^{3+} and Al^{3+} ions at both coordination sites in $Lu_3Al_{5-x}Ga_xO_{12}$:Ce single crystals as a function of Ga content, confirming a pronounced preference of Ga^{3+} for T_d sites, particularly at low Ga concentrations.[39]

Overall, the literature indicates that in garnet single crystals, Ga^{3+} preferentially occupies the smaller T_d sites, while Al^{3+} tends to populate the O_h sites. In contrast, results reported for powder samples remain inconsistent, suggesting that synthesis parameters – such as processing temperature, duration, and preparation route – play a decisive role in determining the final cation distribution within the lattice.

To address these unresolved issues, we present a systematic investigation combining X-ray powder diffraction with Rietveld refinement and solid-state NMR spectroscopy for a series of $Y_3Al_{5-x}Ga_xO_{12}$:Pr garnet samples (x = 0, 1, 2, 2.5, 3, 3.5, 4, 5) synthesized using a Li_2SO_4-flux-assisted route at a moderate temperature of 1300 °C. These experimental data will be confronted with theoretical calculations. The luminescent thermometric performance of this series of materials has been demonstrated previously, revealing a pronounced influence of Ga incorporation on the electronic level structure of the host lattice and, consequently, on its emission properties.[15] The use of Li_2SO_4 flux, which melts at approximately 845 °C, promotes efficient interdiffusion of the constituent oxides and is therefore expected to facilitate cation redistribution toward thermodynamic equilibrium in the final products, despite the moderate synthesis temperature.

2. Experimental

2.1. Materials and synthesis

The powder materials of $Y_3(Al_{5-x}Ga_x)O_{12}$:Pr (x = 0, 1,2, 2.5, 3, 3.5, 4, 5) were synthesized at 1300 °C using stoichiometric mixtures of metal oxides: Y_2O_3 (Stanford Materials, 5N), Al_2O_3 (Roth, 4N5), Ga_2O_3 (AbCr, 4N), and Pr_6O_{11} (Stanford Materials, 5N) with the aid of Li_2SO_4 flux (Alfa Aesar, 99.7%). The mixture was heated in air in a corundum crucible covered with a lid, and after cooling, the product was recovered by washing with hot distilled water several times, followed by acetone. Further details are provided in.[15] The Pr^{3+} nominal content was 0.1 mol% with respect to Y^{3+} in all samples. The crucibles we used were $\sim$2 × 6 cm (diameter x height). We found in numerous experiments that narrow, tall crucibles are much better than short, broad ones. The former greatly impeded the loss of Ga from the reacting mixture and, consequently, from the final garnets.

2.2. Characterization techniques

X-ray diffraction (XRD) patterns were measured using a D8 Advance X-ray diffractometer operating in Bragg–Brentano geometry. Cu $K_{\alpha1}$ radiation (λ = 1.54056 Å), filtered through a Ni filter, was generated at 40 kV and 30 mA. Diffractograms were recorded over a 2θ range of 10–70°, with a step of 0.05° and an acquisition time of 5 s per step. Rietveld refinements were performed for the $Y_3Al_{5-x}Ga_xO_{12}$ compositions (x = 0, 1, 2, 2.5, 3, 3.5, 4, 5) using the EXPGUI interface in conjunction with the GSAS software package. A shifted Chebyshev polynomial function was employed to model the background.

The microstructure of the powders was examined using scanning electron microscopy (SEM) with a Hitachi S-3400N.

Magic-Angle-Spinning NMR ^{27}Al MAS NMR spectra were acquired with a MAS rotation speed of 25 kHz, at a temperature of 300 K, using a 90° pulse of 2 μs, a delay time of 2 s, and 128 scans. Static ^{71}Ga NMR static solid state NMR spectra were acquired at 300 K using a 90° pulse of 1 μs, a delay time of 5 s, and 1000 scans. Pulses were optimized by standard samples of $Al(NO_3)_3$ and $Ga(NO_3)_3$ for ^{27}Al and ^{71}Ga nuclei, respectively.

Compositional analysis of Y, Al, and Ga was performed using a Bruker Tracer 5 XRF spectrometer working under the voltage of 15 kV and the current of 8.45 μA. No filter was used. The acquisition time was 60 s; each sample was analyzed 3 times, and the average value was used in the calculations.

Luminescence spectra were recorded upon 280 nm radiation excitation within 10–700 K on an FLS 1000 spectrometer from Edinburgh Instruments Ltd equipped with a 450 W Xe arc lamp for continuous excitation, double-grating Czerny–Turner monochromators (focal length: 2 × 325 mm) in the excitation and emission compartment, and a thermoelectrically cooled (−20 °C) PMT-980 photomultiplier operating in the 185–900 nm range for light detection. The spectra were corrected for the efficiency of the detection pathway (monochromator gratings' efficiency and photomultiplier sensitivity).

2.3. Computational details

Density functional theory (DFT) calculations employing the PBE exchange–correlation functional[40] were carried out with the AFLOW software[41,42] and the Vienna *ab initio* simulation package (VASP)[43–45] using settings in accordance with the associated AFLOW standard.[46,47] In addition, the internal VASP precision was set to ACCURATE.[48] All geometries were structurally optimized. When substituting one Al within the standard primitive unit cell of the bulk material, Ga and other impurity species in different periodically repeated unit cells are at least 10 Å away from each other.

Importantly, we note that all eight octahedral as well as all twelve tetrahedral sites in the standard primitive unit cell are equivalent. This equivalence then carries over to the Ga substituted structures, such that only one case for the respective coordination needs to be investigated.

3. Results and discussion

3.1. Theoretical calculations

To investigate the selective substitution of Ga^{3+} for Al^{3+} in $Y_3Al_{5-x}Ga_xO_{12}$, DFT calculations were carried out. The Ga^{3+} ions were placed both into a tetrahedral as well as an octahedral site within the standard primitive unit cell (see Fig. 2(a) and (b)). The structures were then fully relaxed. From the energetics, it is found that Ga^{3+} substitution within the octahedral environment is 202 meV/unit cell higher in energy than in the tetrahedral one. This counterintuitive finding with respect to the relative sizes of the host Al^{3+} and guest Ga^{3+} ions can be rationalized by the electronic density of states (DOS) visualized for both cases in Fig. 2(c–f). While the fully occupied Ga d-states are located below −12 eV with respect to the valence band maximum (VBM) in the tetrahedral scenario, they are shifted to higher energies in the octahedral case. This can be understood from the fact that the Ga d-states are more destabilized from coulombic repulsion in the octahedral environment due to the larger number of negatively charged O^{2-} ligands (six) compared to the tetrahedral environment (four). As such, the substitution energetics is thus decisively determined by electronic electrostatic considerations rather than the ion sizes. Although this result is obtained at 0 K, the strong energetic preference clearly dominates any thermal enthalpic effects at the synthesis temperature of 1300 K (equivalent to ∼136 meV).

We note that for the octahedral case, the standard splitting of the d-states into lower t_{2g} and upper e_g orbitals is observed. In the tetrahedral environment, higher order contributions of

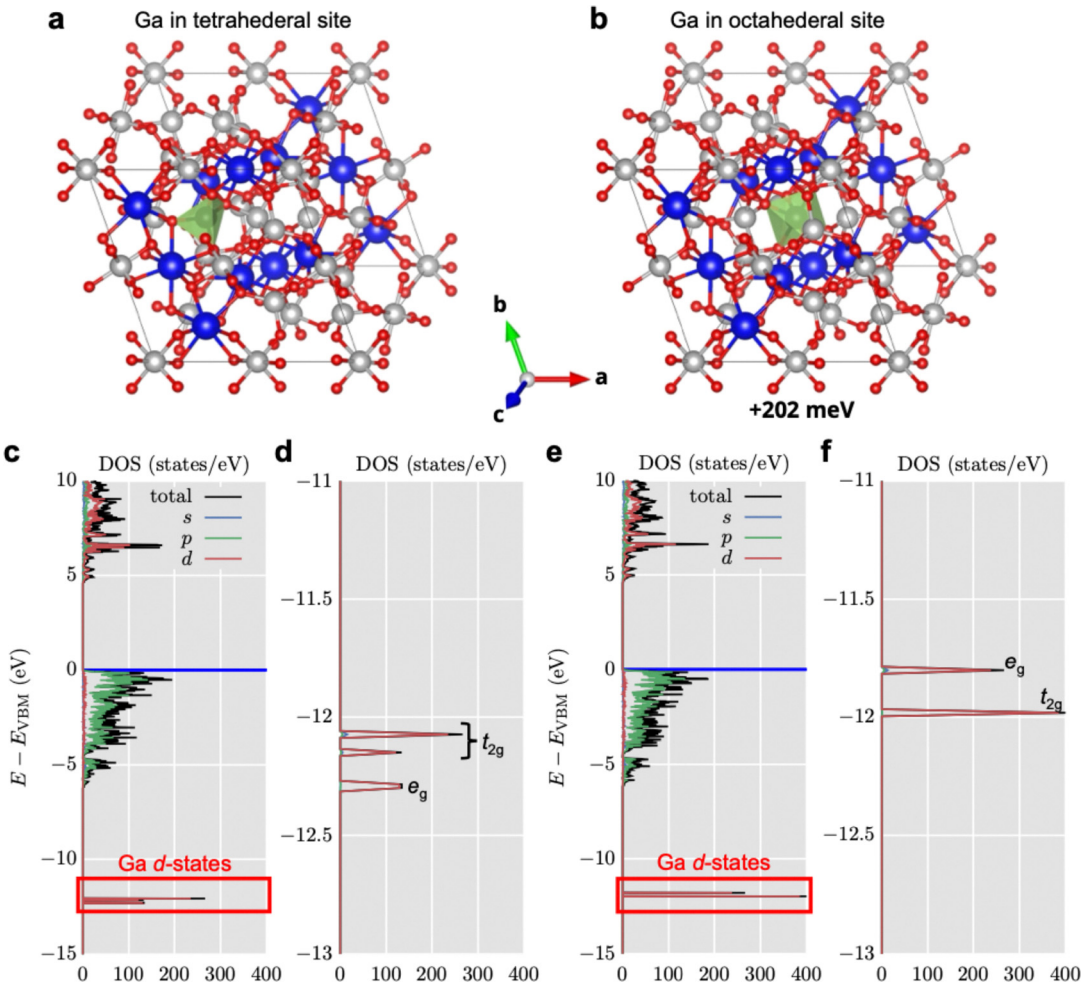

Fig. 2 Ga substitution at different coordination sites. Standard primitive cell with Ga substitution in a tetrahedral (a) or octahedral (b) site. In the latter case, the total energy relative to tetrahedral substitution is indicated below. The substitution sites are marked by the green polyhedra. Colors: Al, light gray; O, red; Y, blue, and Ga, black (in the center of green polyhedra). Electronic DOS for the tetrahedral/octahedral case (c) and (e). The energy is aligned at the VBM. The red frame highlights the position of the Ga d-states. A zoomed view of the respective energy region of these orbitals is depicted in d and f. The states are labeled with the conventional group theoretical symbols.

This journal is © The Royal Society of Chemistry 2026

the crystal field slightly split the formally degenerate upper t_{2g} states.

To investigate and highlight things in a broader context, we have also theoretically examined substitution with other elements of the same group. These results, which formally go beyond the main topic of this paper, may be useful in related research. When replacing Al^{3+} by B^{3+}, the tetrahedral site is clearly preferred by 4077 meV relative to the octahedral one, which can be assigned to the small size of the boron ion. However, when substituting In^{3+}, the octahedral site is preferred by 559 meV, hinting at the increasing importance of relative ion sizes. Eventually, for Tl^{3+} substitution, also the octahedral environment is preferred, but only by 114 meV. Hence, the substitution behavior when investigating a wider range of species is determined by a complex interplay of electronic, electrostatic, and ionic size effects, offering interesting prospects for selective ion substitution in garnet structures. On the other hand, this comparison shows the complexity of this process and proves that simple intuitive analysis can easily fail and lead to erroneous conclusions.

3.2. XRD data, Rietveld analysis, and powders' morphology, and XRF compositional analysis

The XRD patterns of YAGG:Pr samples are presented in Fig. 3a. With no extraneous lines compared to literature data (ICSD #16825, #14343),[49,50] the results confirm single garnet phases for each composition. With increasing Ga content, coherent with the literature, the reflection peaks shifted toward lower angles, indicating an increase in the cubic unit cell. For the (Al,Ga) mixed compositions, especially those with similar content of both these metals, a substantial broadening of the diffraction lines is observed. This indicates an increasing distortion of the crystal structure, as expected, given the difference in the sizes of Al^{3+} and Ga^{3+} ions.

The diffraction patterns were simulated using Rietveld refinement.[51,52] The results are summarized in the SI file. Table S1 summarizes the Rietveld refinement data of $Y_3Al_{5-x}Ga_x$-O_{12}:Pr (x = 0, 1, 2, 2.5, 3, 3.5, 4, 5) series of phosphors, and Table S2 presents the atomic positions and occupancies of the O_h (16a) and T_d (24d) sites by Al and Ga derived for these compositions. Fig. S1–S8 show the quality of the Rietveld fits for the materials. For each sample, good agreement between experiment and model was achieved, with Rb values in the range of 4–6%. The calculated cell parameter, a, of the cubic garnet is shown in Fig. 3b (red) and compared with database values (black). The increase in cell size with increasing Ga content is attributed to the difference in ionic radii between Ga^{3+} and Al^{3+} ions (Ga^{3+}: 0.47 Å in tetrahedral, 0.62 Å in octahedral site; Al^{3+}: 0.39 Å and 0.535 Å, respectively).[16] Overall, the agreement between our results and the database is very good; only for x = 4 does the unit-cell size exceed the literature value by a larger margin. Measurements of a newly synthesized material with this composition confirmed this deviation, yielding essentially identical results. For x = 2.5 and 3.5, no database data are available. However, the nearly linear dependence of $a(x)$ (cubic unit-cell parameter *versus* x) indicates that the agreement is also very good for these compositions.

A plausible explanation for this behavior may lie in local structural distortions or subtle changes in the cation distribution (*e.g.*, Al/Ga ordering on octahedral and tetrahedral sites and/or increased population of antisite defects, which are frequently observed in garnets) specific to this high Ga content. However, a comprehensive understanding of the underlying thermodynamic and kinetic factors would require an extensive, dedicated study involving systematic variations of the synthesis parameters (such as temperature and annealing times) combined with complementary local-structure probes, such as

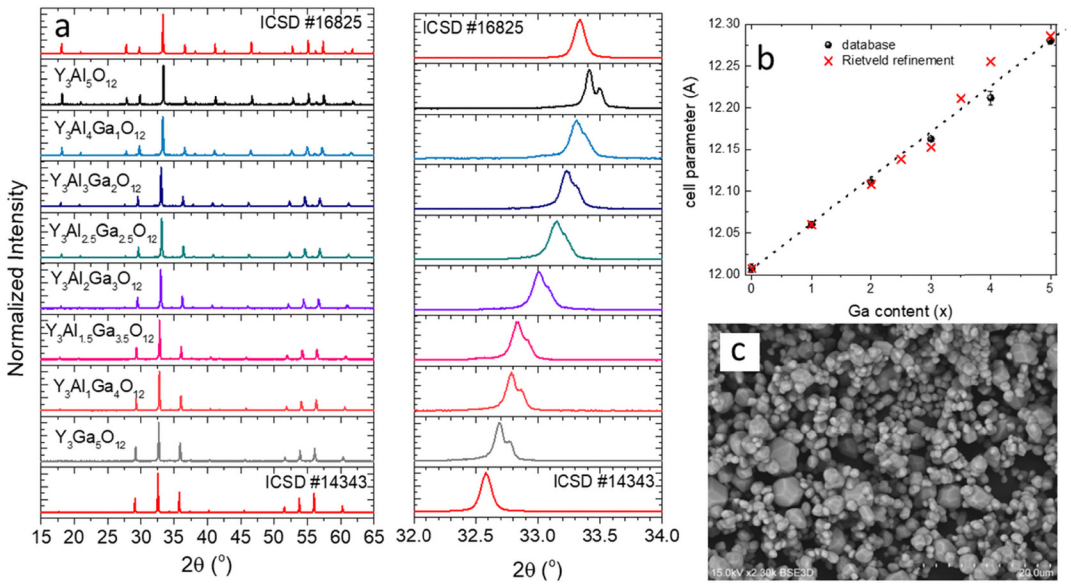

Fig. 3 (a) XRD patterns of YAGG:Pr samples, (b) cell parameter, a, of the cubic garnet phase as a function of the Ga content, (c) typical morphology of the powders. The broken line in (b) is intended only to guide the eye but may also be understood as representing Vegard's law.[53,54]

Raman spectroscopy. This investigation, while highly intriguing, remains beyond the scope of the present paper and will be addressed in future work.

The SEM image presented in Fig. 3c is representative of all samples. It reveals that the powders consist of well-developed, non-agglomerated grains with very similar shapes and sizes, predominantly in the 1–2 μm range. Only a small fraction of larger grains with diameters of 3–4 μm is observed. Since the powders were not milled after synthesis, the grains can be regarded as freely grown due to the presence of the Li_2SO_4 flux. Consequently, these powder phosphors may be considered quite close to single-crystal-like materials in terms of their growth mechanism. However, the much lower temperature compared to crystal pulling (1300 °C *vs.* almost 2000 °C) creates thermodynamically significantly different conditions for grain formation.

As stated above, the vast majority of unagglomerated monocrystalline grains remain within the narrow 1–4 μm range. Although further optimization of the synthesis parameters could yield a highly monodisperse particle size distribution, the current morphology is sufficiently uniform to ensure reliable characterization. Consequently, the structural and optical properties observed herein allow for robust and highly representative physical conclusions to be drawn.

Fractional parameters of Ga ($f_{Ga(IV)}$) and Al ($f_{Al(IV)}$) in the T_h site were calculated based on the data from Rietveld refinement (Fig. 4). For these calculations, occupancy of Ga and Al in T_h and O_h sites was taken into account, and the following formulas, proposed by Laguta *et al.*, were used, eqn (2):[29]

$$f_{Ga(IV)} = \frac{Ga(IV)}{Ga(IV) + Ga(VI)} \quad f_{Al(IV)} = \frac{Al(IV)}{Al(IV) + Al(VI)}, \quad (2)$$

where Ga(IV)/Al(IV) and Ga(VI)/Al(VI) represent Ga/Al in T_h and Ga/Al in O_h site, respectively. The results for all $Y_3Al_{5-x}Ga_xO_{12}$:Pr powders are presented in Fig. 4.

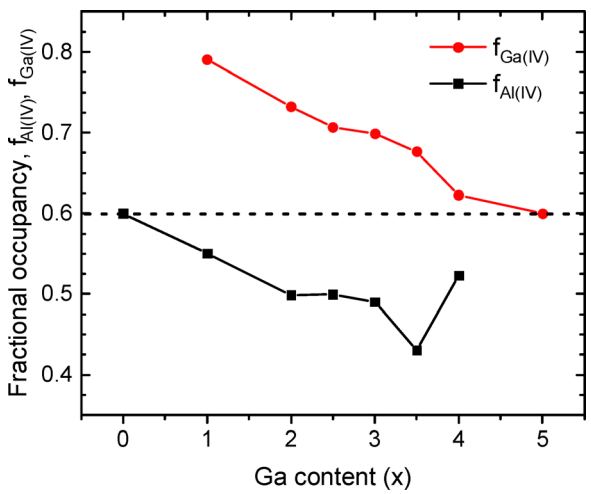

Fig. 4 Fractional occupation parameters of T_d sites of Al^{3+} and Ga^{3+} ions in the $Y_3Al_{5-x}Ga_xO_{12}$:Pr powders. The dotted line represents a random distribution of Al and Ga in T_d and O_h sites. For the definition of the fractional occupancies, see eqn (1).

Within the $Y_3Al_{5-x}Ga_xO_{12}$:Pr powder series, the fractional occupancy parameter of Ga at the tetrahedral (T_d) site, $f_{Ga(IV)}$, exceeds the value expected for a random distribution (0.6) for all compositions. However, it gradually decreases with increasing Ga content, from 0.79 for $Y_3Al_4Ga_1O_{12}$:Pr to 0.62 for $Y_3(Al_1Ga_4)O_{12}$:Pr. A parallel trend is observed for $f_{Al(IV)}$, yet its values remain below 0.6 in all samples, indicating an underrepresentation of Al at the tetrahedral site. Specifically, $f_{Al(IV)}$ decreases from 0.55 for $Y_3(Al_4Ga_1)O_{12}$:Pr to 0.52 for $Y_3(Al_1Ga_4)O_{12}$:Pr.

Notably, the sample with $x = 4$ deviates from this monotonic trend, as its $f_{Al(IV)}$ value (0.52) is significantly higher than that observed for $x = 3.5$ (0.43). Nevertheless, XRD analysis consistently indicates that the larger Ga^{3+} ion (compared to Al^{3+}) preferentially occupies the smaller T_d site rather than the O_h site in $Y_3Al_{5-x}Ga_xO_{12}$:Pr powders synthesized at 1300 °C in the presence of a Li_2SO_4 flux. This preference should not be overinterpreted, as both Ga^{3+} and Al^{3+} share between T_d and O_h sites across all compositions. However, the tetrahedral position clearly exhibits a higher affinity for Ga^{3+} than for Al^{3+}.

The XRF compositional analysis showed that the Y:Al:Ga ratio is in good agreement with the formal composition. Fig. S9 shows that the experimental Al and Ga contents are in good agreement with the theoretical composition of the $Y_3Al_{5-x}Ga_xO_{12}$:Pr garnet series. As we mentioned in the Materials and synthesis section, this was achieved by using tall, narrow crucibles during processing.

3.3. Solid-state NMR data and their analysis

To gain deeper insight into the occupancy of the O_h and T_d sites by Al^{3+} and Ga^{3+}, and to assess their local structures, ss-NMR was performed. It is known that quadrupolar nuclei (such as ^{27}Al and ^{71}Ga) with spin $I > 1/2$, are not spherical but possess an ellipsoidal charge distribution. This generates a nuclear quadrupole moment that interacts with the local electric field. The strength of the interaction between the nuclear quadrupole moment and the electric field gradient (EFG) for a certain nucleus site is given by the quadrupole constant C_q. The EFG, in turn, is the spatial variation of the electric field around the nucleus, due to the distribution of electrons and nearby ions. The more asymmetric the site, the larger the EFG. Therefore, a high C_q value indicates an asymmetric local environment (strong EFG) or a nucleus with a large quadrupole moment.[55,56] C_q is described by eqn (3):

$$C_q = \frac{eQV_{ZZ}}{h}, \quad (3)$$

where e is the electron charge, Q is the nuclear quadrupolar momentum, V_{ZZ} is the major component of the electric field gradient (EFG) tensor, and h is the Planck constant.

Another important quadrupolar interaction parameter is the asymmetry parameter (η), which is an indication of how far from cylindrical symmetry the electric field gradient (EFG) is at the point where the nucleus is located. The expression of η is

 This journal is © The Royal Society of Chemistry 2026

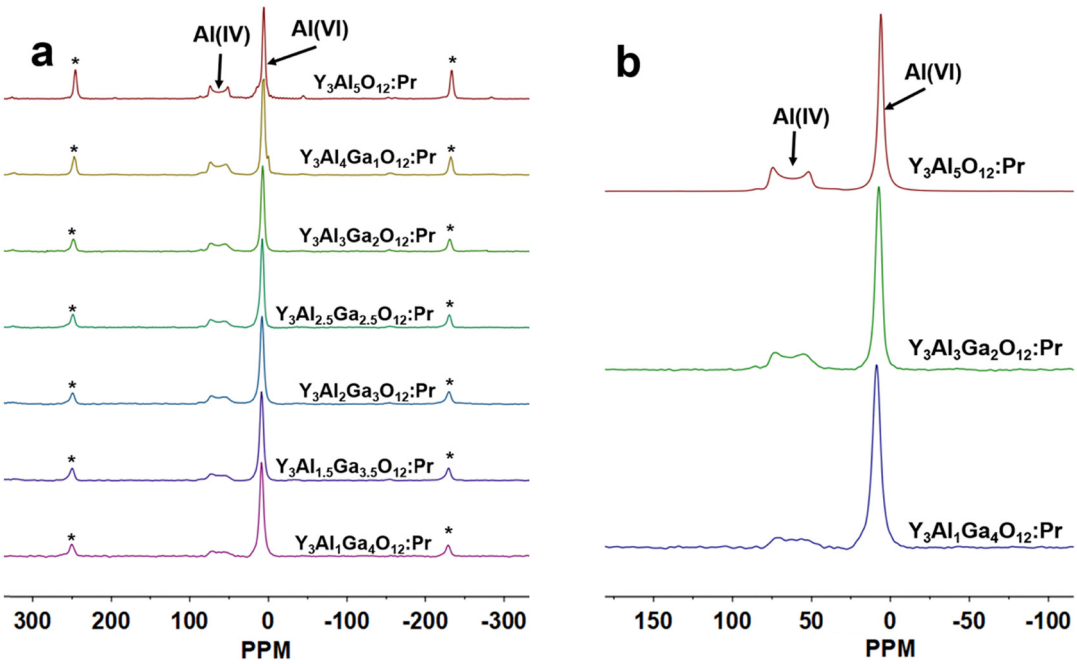

Fig. 5 (a) ^{27}Al MAS NMR of all samples at 25 kHz MAS speed, Al(VI) and Al(IV) resonances are indicated by arrows (asterisks indicate spinning sidebands). (b) ^{27}Al MAS NMR of $Y_3Al_5O_{12}$:Pr, $Y_3Al_3Ga_2O_{12}$:Pr and $Y_3Al_1Ga_4O_{12}$:Pr samples.

given by eqn (4):

$$\eta = \frac{V_{XX} - V_{YY}}{V_{ZZ}}, \quad (4)$$

where $0 \leq \eta \leq 1$ indicates $|V_{ZZ}| \geq |V_{YY}| \geq |V_{XX}|$.

The ^{27}Al MAS NMR and ^{71}Ga static NMR spectra of the $Y_3Al_{5-x}Ga_xO_{12}$:Pr powders are presented in Fig. 5. ^{27}Al MAS NMR spectra of all the investigated samples show two well-defined signals, evidenced by arrows in Fig. 5, due to aluminum in O_h and T_d sites (Al(VI) and Al(IV) at 1.2 and 78 ppm, respectively. The spectra analysis allowed obtaining the isotropic chemical shift (δ_{iso}) and the quadrupolar interaction parameters (quadrupolar constant (C_q) and asymmetry parameter (η)).

The presence of the two signals, both with η = 0 in all spectra, indicates that Al occupies both sites in all samples. However, some important differences are evident. Firstly, as the Ga content increases, the second-order quadrupolar shape of the signal due to the T_d site at 78 ppm loses sharpness (Fig. 5b), indicating an increase in the distribution of electric field gradients. Nevertheless, the quadrupolar constant remains unchanged. On the other hand, as shown in Fig. 6, the resonance of the O_h site is characterized by a very sharp signal and by a sideband pattern.

The sideband patterns spread over a spectral window of around 250 kHz for the $Y_3Al_5O_{12}$:Pr sample and around 400 kHz for the $Y_3Al_1Ga_4O_{12}$:Pr sample. Furthermore, the Al(O_h) site quadrupolar constant and chemical shift values increase with the Ga content (Fig. 7). These are all evidences that a progressive distortion of the O_h site as the Ga content increases takes place, and this substantiates the preference of Al in the O_h coordination. This was further confirmed by analysis of the signal area ratios, from which an increase of the Al occupying O_h sites from around 65–70% to 86% was found.

In order to confirm this finding, the investigation of ^{71}Ga static NMR spectra was performed, in which the signal corresponding to the tetrahedral site broadens and increases in intensity with increasing gallium content. In details, the ^{71}Ga static NMR spectra shown in Fig. 8 present two large, superimposed resonances, as indicated by the checkboxes, due to Ga in T_d and O_h coordination for all samples (Fig. 8a). The fitting of each band was performed in order to evaluate the chemical shift (δ) and the quadrupolar constant (C_q) as a function of Ga content (Fig. 8b). Even in this case, for both sites, the asymmetry parameter η is around zero, indicating a cylindrical shape of the electric field gradient around these sites. It is worth noting that the signal from the T_d site broadens and increases in intensity, while the ^{71}Ga quadrupolar parameters (η and C_q) remain unchanged for all samples. On the other hand, an increase in the C_q values for the O_h site as the Ga content rises is observed (see Fig. 8a). These are all harmonious evidences of the Ga preference for the tetrahedral site. Let us emphasize that this is a preference, and that both Ga and Al share the available T_h and O_h coordination sites, as is evident from the data presented. The effect is most pronounced at the beginning of the $Y_3Al_{5-x}Ga_xO_{12}$:Pr series (low x values) but is observed across the composition range.

4. Phonon-driven energy flow in YAGG series

The understanding of how lattice modifications influence the evolution of the phonon spectrum – and, consequently,

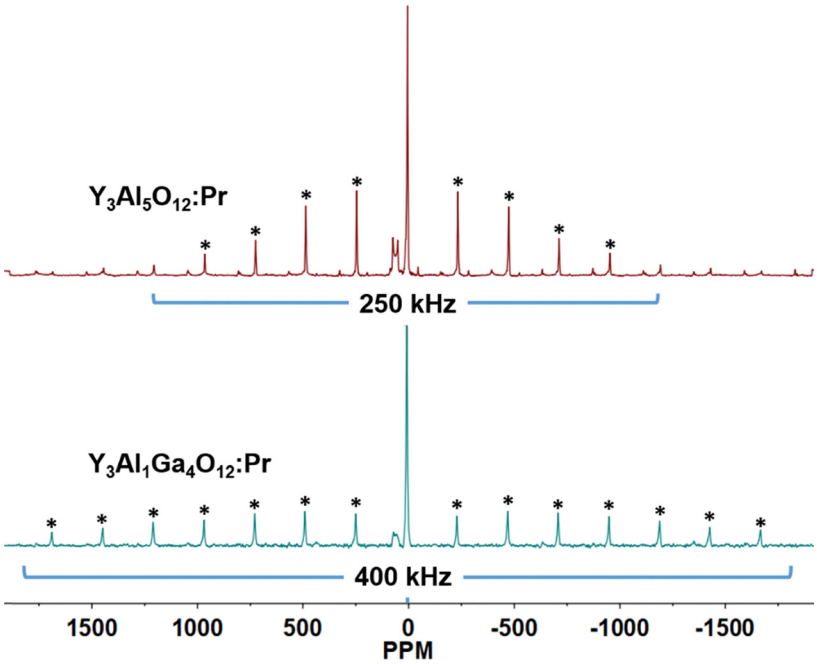

Fig. 6 ^{27}Al MAS NMR of $Y_3Al_5O_{12}$:Pr and $Y_3Al_1Ga_4O_{12}$:Pr samples (asterisks indicate spinning idebands).

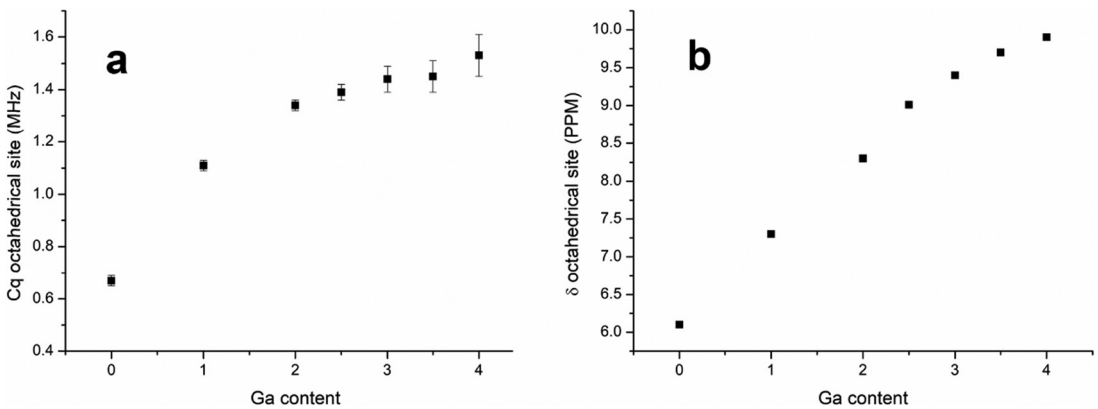

Fig. 7 ^{27}Al quadrupole coupling constant (a) and chemical shift (b) of the octahedral site.

the luminescence properties of otherwise similar systems – is central to this study. Therefore, we demonstrate in this final stage how potent the effects of continuous Al substitution by Ga are in $Y_3Al_{5-x}Ga_xO_{12}$:Pr phosphors.

Fig. 9 presents the evolution of the luminescence spectra in the range of the $^3P_0 \rightarrow {}^3H_4$ (around 490 nm) and the $^1D_2 \rightarrow {}^3H_4$ transitions (approx. 605–610 nm). The most striking effect in the $Y_3Al_{5-x}Ga_xO_{12}$:Pr series is the reversal of dominant emission: in Ga-free $Y_3Al_5O_{12}$:Pr, the red $^1D_2 \rightarrow {}^3H_4$ luminescence strongly dominates the $^3P_0 \rightarrow {}^3H_4$ emission over the entire investigated temperature range (15–700 K). In $Y_3Al_4Ga_1O_{12}$:Pr, the red emission prevails, though its dominance is radically reduced, especially below 400 K. Above 500 K, the $^3P_0 \rightarrow {}^3H_4$ emission declines rapidly, while the $^1D_2 \rightarrow {}^3H_4$ luminescence exhibits higher resistance to thermal quenching, which makes its intensity strongly dominant again. In contrast, in $Y_3Al_3Ga_2O_{12}$:Pr, the $^3P_0 \rightarrow {}^3H_4$ transition already yields more (greenish-blue) light than the $^1D_2 \rightarrow {}^3H_4$. As the Ga content increases further, the $^3P_0 \rightarrow {}^3H_4$ emission becomes predominant and eventually dominates the spectrum.

Thus, the trend is clear: increasing the Ga content in the host reduces the nonradiative energy flow from $^3P_0$ to $^1D_2$, thereby enhancing the efficiency of $^3P_0$ emission at the expense of $^1D_2$ luminescence. This effect, profound even when only one out of five Al^{3+} ions is replaced with Ga^{3+}, is consistent with the XRD and NMR data discussed above. Because Ga favors the tetrahedral sites, which host the most energetic vibrations governing nonradiative multiphonon relaxation, even minor Ga additions quickly reduce the availability of these high-energy phonons and downgrade the feeding of $^1D_2$ from $^3P_0$.

 This journal is © The Royal Society of Chemistry 2026

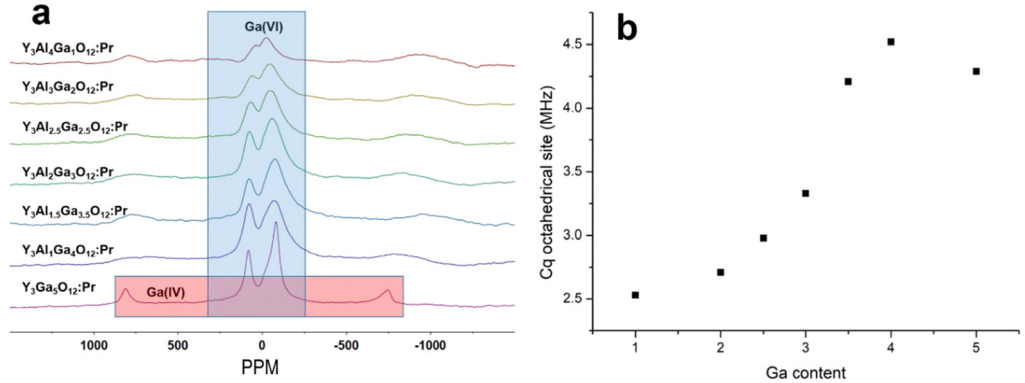

Fig. 8 (a) ^{71}Ga static NMR spectra of YAGG:Pr samples. Blue and red checkboxes indicate Ga in O_h and T_d coordination signals, respectively. (b) ^{71}Ga quadrupole coupling constant for the octahedral site.

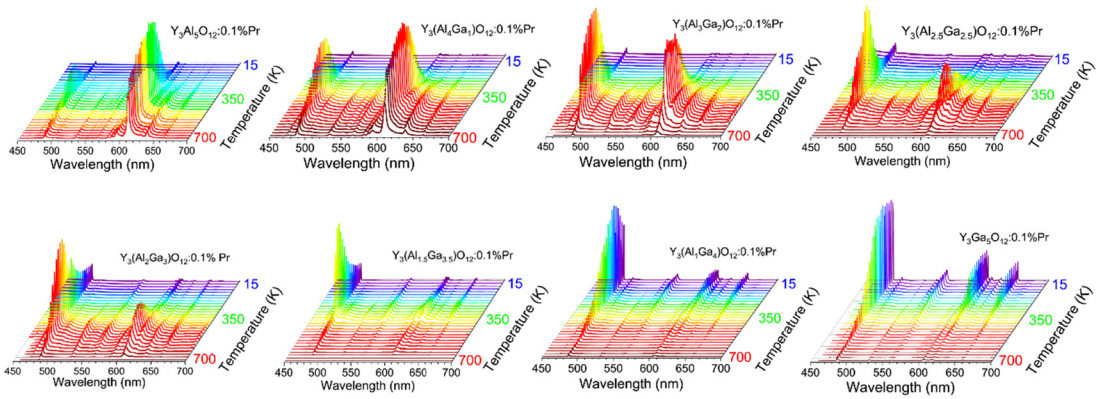

Fig. 9 Spectral evolution of $Y_3Al_{5-x}Ga_xO_{12}$:Pr luminescence (Exc. = 280 nm) showing the $^3P_0 \rightarrow {}^3H_4$ (~490 nm) and $^1D_2 \rightarrow {}^3H_4$ (~605–610 nm) transitions. The systematic Ga substitution results in a pronounced inhibition of the non-radiative energy flow from the $^3P_0$ to the $^1D_2$ level. See text for a detailed discussion.

5. Discussion and conclusions

The experimental evidence for the preferential tetrahedral site occupancy of Ga^{3+} in $Y_3Al_{5-x}Ga_xO_{12}$:Pr is striking. While a purely statistical distribution would yield a 60% occupancy for the tetrahedral sites, our XRD and NMR data reveal a significant enrichment, with approximately 80% of the initial Ga^{3+} substituents preferentially entering these positions. This "excess" occupancy at the beginning of the series explains why even minor Ga^{3+} addition leads to a disproportionately large increase in $^3P_0$ luminescence relative to $^1D_2$ emission. By targeting the tetrahedral sites – which host the highest energy lattice phonons (~900 cm^{-1}) – Ga effectively suppresses the primary non-radiative pathway. The reduction in available high-energy vibrations increases the multi-phonon order required to bridge the ~3500 cm^{-1} energy gap between $^3P_0$ and $^1D_2$, thereby reducing the non-radiative rate (as described by eqn (1)) and shifting the dominant emission from the red ($^1D_2$) to the greenish-blue ($^3P_0$) region.

Ultimately, this series serves as a compelling reminder that physical intuition must be tempered by rigorous structural verification. At first glance, one might expect the larger Ga^{3+} ion ($r(T_d)$ = 0.47 Å) to avoid the smaller tetrahedral site in favor of the larger octahedral one, especially when compared to the smaller Al^{3+} ($r(T_d)$ = 0.39 Å). However, our results confirm that the distinct preference of Ga for tetrahedral coordination has profound consequences. This demonstrates that in complex lattices, local site preference can be more influential than global concentration, acting as the primary lever in determining the efficiency and color purity of the phosphor.

As noted in the Introduction, previous research has yielded conflicting conclusions regarding Ga distribution. We deduce that the Ga^{3+} partitioning in $Y_3Al_{5-x}Ga_xO_{12}$ is highly sensitive to fabrication conditions – specifically the thermal history and the resulting proximity to thermodynamic equilibrium. A comparable phenomenon has been reported for Eu^{3+} ions in Lu_2O_3.[57] This matrix offers non-centrosymmetric C_2 (75%) and centrosymmetric C_{3i} sites (25%; often referred to as S_6 in spectroscopic literature, though C_{3i} is the correct crystallographic notation). Rapid combustion synthesis results in random occupancy (75% in C_2, 25% in C_{3i} sites), whereas high-temperature annealing (1750 °C) for a few hours induces a significant redistribution toward a new equilibrium (85% C_2, 15% C_{3i}

sites). We infer that a similar kinetic-*versus*-thermodynamic competition likely explains the discrepancies in literature reports for garnet hosts. Consequently, processing parameters must be recognized as a vital factor in shaping the atomic architecture of mixed-cation host lattices.

Author contributions

EZ and MLS: conceptualization and methodology. PB: NP preparation, XRD, and optical properties. AS: ss-NMR investigation. RF: theoretical analysis and computation, MS: Rietveld analysis, reviewing. PB, AS, MLS, EZ, and RF: writing, reviewing, and editing. All authors contributed to the article and approved the submitted version.

Conflicts of interest

The authors declare that they have no known competing financial interests or personal relationships that could have appeared to influence the work reported in this paper.

Data availability

The datasets generated and/or analyzed during the current study are available at https://doi.org/10.34616/llknj4.

Supplementary information (SI) contains the Rietveld refinement data and the results of the XRF analysis. See DOI: https://doi.org/10.1039/d6tc01758d.

Acknowledgements

ss-NMR experimental data were provided by ATeN Center – University of Palermo (https://www.unipa.it/servizi/atencenter). MLS thanks the Join Chairs Project 'Innovative Nanostructured Materials with Luminescent Properties for Cultural Heritage (NanoLuBC)' – Document No. 184 of 14/05/2024 by the CNR Board of Directors. Prot. No. 73332 – 06/05/2025. Contracts and Agreements Register No. 2175/2025. EZ acknowledges financial support by the National Science Centre Poland, under grant #UMO-2023/51/B/ST5/02341. RF acknowledges funding by the German Research Foundation (DFG), project FR 4545/2-1, collaborative research center SFB 1415, Project C08, Project ID 417590517, and for the ''Autonomous Materials Thermodynamics'' (AutoMaT) project by Technische Universität Dresden and Helmholtz-Zentrum Dresden-Rossendorf within the DRESDEN-concept alliance. The authors thank the HZDR Computing Center, HLRS Stuttgart, the Paderborn Center for Parallel Computing PC2, and TU Dresden ZIH for generous grants of CPU time.

References

1 J. Xu and S. Tanabe, *J. Lumin.*, 2019, **205**, 581–620.
2 J. Xu, S. Tanabe, A. D. Sontakke and J. Ueda, *Appl. Phys. Lett.*, 2015, **107**(8), 081903.
3 S. Feng, H. Qin, G. Wu, H. Jiang, J. Zhao, Y. Liu, Z. Luo, J. Qiao and J. Jiang, *J. Eur. Ceram. Soc.*, 2017, **37**, 3403–3409.
4 V. Boiko, Z. Dai, M. Markowska, C. Leonelli, C. Mortalò, F. Armetta, F. Ursi, G. Nasillo, M. L. Saladino and D. Hreniak, *Sci. Rep.*, 2021, **11**, 1–14.
5 Q. Du, J. Ueda and S. Tanabe, *J. Mater. Chem. C*, 2023, **11**, 16225–16233.
6 Q. Du, J. Ueda and S. Tanabe, *J. Ceram. Soc. Jpn.*, 2024, **132**, 116–120.
7 J. Xu, J. Ueda and S. Tanabe, *J. Mater. Chem. C*, 2016, **4**, 4380–4386.
8 Y. Zorenko, V. Gorbenko, V. Savchyn, T. Zorenko, A. Fedorov, H. Wrzesinski and Y. Vasylkiv, *Radiat. Meas.*, 2013, **56**, 150–154.
9 E. Zych, C. Brecher and H. Lingertat, *J. Lumin.*, 1998, **78**, 121–134.
10 Z. Dai, V. Boiko, K. Grzeszkiewicz, M. Markowska, F. Ursi, J. Hölsä, M. L. Saladino and D. Hreniak, *Opt. Mater.*, 2021, **111**, 110522.
11 Y. Zorenko, V. Gorbenko, V. Savchyn, T. Zorenko, A. Fedorov and O. Sidletskiy, *IEEE Trans. Nucl. Sci.*, 2014, **61**, 439–442.
12 Y. Zorenko, V. Gorbenko, T. Zorenko and Y. Vasylkiv, *Opt. Mater.*, 2014, **36**, 1760–1764.
13 D. Chen, Y. Zhou, W. Xu, J. Zhong and P. Huang, *J. Mater. Chem. C*, 2016, **4**, 11457–11464.
14 J. Ueda, M. Katayama, K. Asami, J. Xu, Y. Inada and S. Tanabe, *Opt. Mater. Express*, 2017, **7**, 2471.
15 P. Bolek, J. Zeler, C. D. S. Brites, J. Trojan-Piegza, L. D. Carlos and E. Zych, *Chem. Eng. J.*, 2021, **421**, 129764.
16 R. D. Shannon, *Acta Crystallogr. Sect. A*, 1976, **32**, 751–767.
17 K. Takagi, M. Yamaga, E. G. Villora, K. Shimamura, K. Hasegawa, H. Ito, S. Mizuno, Y. Takeda and T. P. J. Han, *J. Lumin.*, 2016, **169**, 65–71.
18 K. Asami, J. Ueda, M. Kitaura and S. Tanabe, *J. Lumin.*, 2018, **198**, 418–426.
19 P. Gluchowski, R. Pązik, D. Hreniak and W. Stręk, *J. Lumin.*, 2009, **129**, 548–553.
20 M. Nikl, E. Mihokova, J. Pejchal, A. Vedda, Y. Zorenko and K. Nejezchleb, *Phys. Status Solidi*, 2005, **242**, 119–121.
21 M. Nikl, V. V. Laguta and A. Vedda, *Phys. Status Solidi*, 2007, **204**, 683–689.
22 A. Pujats, A. Veispals and J. Jansons, Proc. SPIE 2967, Opt. Inorg. Dielectr. Mater. Devices.
23 J. Ueda, P. Dorenbos, A. J. J. Bos, K. Kuroishi and S. Tanabe, *J. Mater. Chem. C*, 2015, **3**, 5642–5651.
24 J. Luo, Y. Wu, G. Zhang, H. Zhang and G. Ren, *Opt. Mater.*, 2013, **36**, 476–481.
25 P. Dorenbos, *J. Lumin.*, 2019, **214**, 116536.
26 P. Dorenbos, *Opt. Mater.*, 2025, **164**, 117007.
27 P. Dorenbos, *J. Lumin.*, 2024, **267**, 120358.
28 F. Di Quarto, A. Zaffora, F. Di Franco and M. Santamaria, *J. Phys. Chem. C*, 2022, **126**, 17313–17327.
29 V. Laguta, Y. Zorenko, V. Gorbenko, A. Iskaliyeva, Y. Zagorodniy, O. Sidletskiy, P. Bilski, A. Twardak and M. Nikl, *J. Phys. Chem. C*, 2016, **120**, 24400–24408.
30 K. Park, H. Kim, G. W. Jung, D. H. Kim and S. Y. Gwon, *J. Alloys Compd.*, 2022, **921**, 166019.

 This journal is © The Royal Society of Chemistry 2026

31 Y.-C. Lin, P. Erhart and M. Karlsson, *J. Mater. Chem. C*, 2019, **7**, 12926–12934.

32 E. Cavalli, E. Zannoni, M. Bettinelli, A. Speghini, M. Tonelli and A. Toncelli, *J. Phys.: Condens. Matter*, 2000, **12**, 4665–4674.

33 G. Blasse and B. C. Grabmaier, *Luminescent Materials*, Springer-Verlag, Berlin Heidelberg, 1994.

34 S. Fu, J. Tan, X. Bai, S. Yang, L. You and Z. Du, *Opt. Mater.*, 2018, **75**, 619–625.

35 L. Jiang, X. Zhang, S. Zhu, H. Tang, Q. Li, W. Zhang, X. Mi, L. Lu, H. Liu and X. Liu, *J. Mater. Sci.: Mater. Electron.*, 2018, **29**, 9045–9051.

36 F. Armetta, M. Gaboardi, J. Plaisier and M. L. Saladino, *Opt. Mater.*, 2023, **140**, 113896.

37 N. Gautier, M. Gervais, C. Landron, D. Massiot and J.-P. Coutures, *Phys. Status Solidi*, 1998, **165**, 329–336.

38 Y. O. Zagorodniy, V. Chlan, H. Štěpánková, Y. Fomichov, J. Pejchal, V. V. Laguta and M. Nikl, *J. Phys. Chem. Solids*, 2019, **126**, 93–104.

39 V. Babin, M. Buryi, V. Chlan, Y. Fomichov, K. Kamada, V. V. Laguta, M. Nikl, J. Pejchal, H. Štěpánková, A. Yoshikawa, Y. Zagorodniy and S. Zazubovich, *J. Lumin.*, 2018, **200**, 141–150.

40 J. P. Perdew, K. Burke and M. Ernzerhof, *Phys. Rev. Lett.*, 1996, **77**, 3865–3868.

41 M. Esters, C. Oses, S. Divilov, H. Eckert, R. Friedrich, D. Hicks, M. J. Mehl, F. Rose, A. Smolyanyuk, A. Calzolari, X. Campilongo, C. Toher and S. Curtarolo, *Comput. Mater. Sci.*, 2023, **216**, 1–24.

42 S. Divilov, H. Eckert, S. D. Thiel, S. D. Griesemer, R. Friedrich, N. H. Anderson, M. J. Mehl, D. Hicks, M. Esters, N. Hotz, X. Campilongo, A. Calzolari and S. Curtarolo, *High Entropy Alloys Mater.*, 2025, **3**, 178–187.

43 G. Kresse and J. Hafner, *Phys. Rev. B: Condens. Matter Mater. Phys.*, 1993, **47**, 558–561.

44 G. Kresse and J. Furthmüller, *Phys. Rev. B: Condens. Matter Mater. Phys.*, 1996, **54**, 11169–11186.

45 G. Kresse and J. Furthmüller, *Comput. Mater. Sci.*, 1996, **6**, 15–50.

46 C. E. Calderon, J. J. Plata, C. Toher, C. Oses, O. Levy, M. Fornari, A. Natan, M. J. Mehl, G. Hart, M. Buongiorno Nardelli and S. Curtarolo, *Comput. Mater. Sci.*, 2015, **108**, 233–238.

47 G. Kresse and D. Joubert, *Phys. Rev. B: Condens. Matter Mater. Phys.*, 1999, **59**, 1758–1775.

48 R. Friedrich, D. Usanmaz, C. Oses, A. Supka, M. Fornari, M. Buongiorno Nardelli, C. Toher and S. Curtarolo, *npj Comput. Mater.*, 2019, **5**, 1–12.

49 H. S. Yoder and M. L. Keith, *Geol. Soc. Am. Bull.*, 1950, **61**, p1516–p1517.

50 P. Fischer, W. Hälg, E. Stoll and A. Segmüller, *Acta Crystallogr.*, 1966, **21**, 765–769.

51 H. M. Rietveld, *J. Appl. Crystallogr.*, 1969, **2**(2), 65–71.

52 *The Rietveld Method*, ed. R. A. Young, Oxford University Press, 1993.

53 L. Vegard, *Z. Phys.*, 1921, **5**, 17–26.

54 A. R. Denton and N. W. Ashcroft, *Phys. Rev. A: At., Mol., Opt. Phys.*, 1991, **43**, 3161–3164.

55 S. E. Ashbrook and S. Wimperis, *NMR of Quadrupolar Nuclei in Solid Materials*, John Wiley & Sons, Ltd, United States, 2012, pp. 45–61.

56 T. Bräuniger and M. Jansen, *Z. Anorg. Allg. Chem.*, 2013, **639**, 857–879.

57 G. Concas, G. Spano, E. Zych and J. Trojan-Piegza, *J. Phys.: Condens. Matter*, 2005, **17**, 2597–2604.